

Density Functional Theory Study of the Jahn–Teller Effect and Spin–Orbit Coupling for Copper and Gold Trimers

Yinghua Shen and Joseph J. BelBruno*

Dartmouth College, Department of Chemistry, Hanover, New Hampshire 03755

Received: July 21, 2004

The Born–Oppenheimer potential energy hypersurfaces of copper and gold trimers were calculated using density functional theory with an analytic potential. The calculated Jahn–Teller distortion energies, pseudorotation barriers, dissociation, and isomerization energies for the two trimers are discussed. Global minima from the surfaces were optimized using the density functional theory method as well as the coupled cluster-singles-doubles-with-triples energies technique. The agreement of the optimized structures with the analytic potential was very good. The Mulliken population analysis compared favorably with the experimental electron spin resonance results. Spin–orbit coupling was subsequently included and the effect was significant for gold, but negligible for copper. The spin–orbit effect suppressed the Jahn–Teller distortion of the gold trimer, and the potential surface with the spin–orbit effect included was also obtained. The spin–orbit splitting for the D_{3h} geometry of the gold trimer was in excellent agreement with the most recent infrared spectroscopic results.

I. Introduction

Increasing experimental and theoretical research has been devoted, in recent years, to the determination of the properties of small metal clusters in the gas phase. Much effort has been paid to small clusters of the coinage metals, Cu, Ag, and Au. In part, this interest results from their connection to broad practical applications; for example, silver clusters in photographic processes¹ and clusters of all three metals in chemical catalysis.² The trimers are of special interest because they pose classic examples of the Jahn–Teller effect.

The Jahn–Teller effect for some group I_B clusters has been explored experimentally by gas-phase optical spectroscopy^{3–6} (Cu_3 and Ag_3) or matrix-isolated ESR studies (Cu_3 , Ag_3 , Au_3 , and $CuAgCu$ ⁷). In addition, some computational studies have been reported. Among the earliest computational reports are the all-electron studies of Bachmann et al.⁸ for Cu_3 . More recent work includes the singles-plus-doubles configuration-interaction (SDCI) and coupled pair functional (CPF) calculations for Cu_3 by Langhoff et al.,⁹ the local spin density (LSD) work of Flad et al.¹⁰ on Cu_3 and Ag_3 clusters, the MCSCF/Multireference singles+doubles CI (MRSDCI) calculations of Balasubramanian and Liao¹¹ for Au_3 and Ag_3 , the CPF calculations for Cu_3 , Ag_3 , and $AgCu_2$ by Walch et al.¹² and the CCSD calculations for Ag_3 by Yoon et al.¹³ Shen and BelBruno¹⁴ have reported the full ground-state potential surface for the silver trimer.

Although experiments and calculations have been reported for specific trimers from this group of elements, most of them focus on the classical Jahn–Teller effect and ignore spin–orbit coupling (an important exception, the work of Balasubramanian and co-workers,¹⁵ is discussed in the Results). In addition, these studies typically involved only a small part of the configuration space. For example, Balasubramanian and Liao¹⁶ have reported the bending potential for Au_3 . We believe that calculations of the full potential energy surfaces are important for later molecular dynamics simulations and the explanation of some of the spectroscopic results. Because we have already explored

the full potential energy surfaces of Ag_3 ,¹⁴ the primary goal of this work is to report the results of a series of calculations involving the full potential energy surfaces of Cu_3 and Au_3 , including the spin–orbit effect in the two systems. Because high-level ab initio calculations, including very accurate methods such as CCSD(T), are CPU intensive for transition-metal-containing molecules, we chose to use density functional theory methods as the major computational tool. However, selected CCSD(T) results will be provided as comparison points for the DFT results.

The methods used to study the trimers and calibration calculations involving the $X^1\Sigma_g^+$ state of the transition metal dimers will be discussed in the next section. In the Results, we begin with a discussion of the general features of the Born–Oppenheimer (BO) hypersurfaces for the trimers, as well as DFT and ab initio optimizations for the lowest energy configurations. This is followed by the detailed electronic properties of the ground-state geometries and a comparison with available experimental results. Finally, some general conclusions are provided.

II. Methods

The main focus of the calculations involves the application of DFT methods to the trimers Cu_3 and Au_3 . However, it is crucial that there be results available for comparison to judge the accuracy of the DFT methods. There are two components to this comparison: relative accuracy as compared to high-level ab initio techniques and accuracy as measured by comparison to experimental results. The computational methods and the relevant comparisons are discussed below.

a. CCSD(T) Dimer Reference Calculations. The CCSD(T) theoretical method is one of the most accurate single reference, electron correlated ab initio techniques available. To assess the performance of the DFT methods, we have completed CCSD(T) calculations for both dimers and selected electronic states of the trimers. For these calculations, completed using the

TABLE 1: Physical Parameters for Cu₂ as a Function of Theoretical Method^a

basis sets	methods	bond length, Å	frequencies, cm ⁻¹	D _e , eV
TZ2P	LDA	2.182	283.2	2.60
	LDA(rel)	2.153	297.8	2.76
	BLYP(rel)	2.236	262.1	2.17
	PBE(rel)	2.215	271.1	2.26
	PW91(rel)	2.210	272.9	2.25
	RPBE(rel)	2.243	258.9	2.01
	RevPBE(rel)	2.236	261.4	2.03
QZ4P	LDA	2.179	285.3	2.61
	LDA(rel)	2.151	300.2	2.77
	BLYP(rel)	2.238	261.6	2.17
	PBE(rel)	2.219	269.7	2.26
	PW91(rel)	2.213	272.3	2.26
	PW91(rel+spin-orbit)	2.212		2.26
	RPBE(rel)	2.250	255.8	2.02
	RevPBE(rel)	2.242	259.5	2.04
	StECP	CCSD(T)	2.264	253.8
StECP+2f	CCSD(T)	2.226	269.1	1.96
exp ²¹		2.220	264.6	2.03

^a The designation “rel” refers to the inclusion of relativistic effects via the ZORA formalism. The molecular dissociation energies D_e are calculated with respect to the lowest LS state of the atom in the scalar relativistic ZORA case, and the lowest $|JM_J\rangle$ is calculated in the fully relativistic ZORA (spin-orbit ZORA) case.

TABLE 2: Physical Parameters for Au₂ as a Function of Theoretical Method^a

basis sets	methods	bond length, Å	frequencies, cm ⁻¹	D _e , eV
TZ2P	LDA	2.619	145.0	2.49
	LDA(rel)	2.462	192.7	2.90
	BLYP(rel)	2.558	163.9	2.12
	PBE(rel)	2.523	173.2	2.29
	PW91(rel)	2.519	174.5	2.32
	RPBE(rel)	2.548	164.7	2.04
	revPBE(rel)	2.541	167.1	2.06
QZ4P	LDA	2.682	137.2	2.01
	LDA(rel)	2.459	195.4	2.92
	BLYP(rel)	2.554	165.0	2.14
	PBE(rel)	2.519	174.3	2.31
	PW91(rel)	2.514	177.0	2.33
	PW91(rel+spin-orbit)	2.508		2.41
	RPBE(rel)	2.543	166.0	2.05
	revPBE(rel)	2.536	168.2	2.08
	StECP	CCSD(T)	2.574	170.1
StECP+2f	CCSD(T)	2.520	181.6	2.19
exp ²¹		2.472	191	2.31

^a See Table 1 for details.

GAUSSIAN 98 suite of programs,¹⁷ the small-core, energy-consistent relativistic pseudopotentials and corresponding basis sets developed by the Stuttgart group (StECP)^{18,19} were employed. In this pseudopotential, the inner shell (core) electrons are replaced by an effective potential and the 19 remaining electrons ($ns^2np^6nd^{10}(n+1)s^1$) are explicitly treated as valence electrons. It has been reported in the literature that inclusion of f functions is critical to the final accuracy of calculations involving transition metal clusters.^{12,20,21} Therefore, we have supplemented the basis set with two f functions not normally included. These additional f functions were optimized using the ground-state energy of the Cu and Au atoms. The effect of this extended basis set may be measured by examining the physical properties of the transition metal dimers shown in Tables 1 and 2. The results in the last three rows of each table indicate that the inclusion of the f functions significantly improves the agreement between the calculated and experimental results (bond length, binding energy, and harmonic frequency).

The CCSD(T)/StECP(2f) theoretical method was also employed to generate comparison data for selected trimer electronic states. However, the ${}^2E'$ state is not included in this set of results. Both the singly occupied HOMO and the LUMO belong to the e' representation in D_{3h} symmetry. A single reference method such as CCSD(T) cannot adequately treat this system. This exact difficulty was evident in several earlier studies involving the trimers of silver¹³ and group V trimers.²² Because of the multiconfigurational nature of the ground state as well as the splitting of that state into Jahn–Teller components, reduced (C_{2v}) symmetry was employed in the previous calculations. This is the approach in the current work as well.

b. Comparison of DFT Theoretical Methods. Calculations for the BO hypersurfaces and geometry optimizations of global minima were completed using the Amsterdam Density Functional (ADF) 2002.02 software package.²³ Test calculations involving homo-dimers of the two metals were used to determine appropriate computational parameters for the trimer studies. The available experimental data for the dimers provide an appropriate comparison point to judge the effectiveness of the candidate DFT computational techniques. The relativistic effect is the first issue to be addressed. It is well-known that calculations involving transition metals, especially heavy transition metals such as gold, require explicit inclusion of relativistic effects.²⁴ Among the relativistic correction methods, the Zero Order Regular Approximation (ZORA)^{25–29} generally provides better results than does the Pauli formalism, especially for the heaviest elements. The ZORA formalism includes mass–velocity corrections found in the quasi-relativistic Pauli approximation but is variationally bound in regions of space where the Pauli approximation fails. For this reason, the ZORA formalism and the ZORA basis set in ADF, which is optimized for use with the ZORA method, were used for all relativistic calculations. Because preliminary calculations indicated that the frozen core approximation affects the spin–orbit splitting in Au₃, we chose to use all-electron basis sets. In the ZORA basis set directory, there are two all-electron basis sets. One is the TZ2P basis set, which is core double- ζ , valence triple- ζ and includes double polarization functions. The other is the QZ4P basis set. It may be described as core triple- ζ and valence quadruple- ζ with four sets of polarization functions. With the TZ2P basis set, the basis functions may be represented as (9s, 6p, 3d, 1f) for Cu and (14s, 10p, 7d, 4f) for Au. In the QZ4P basis set, the basis functions for Cu are (14s, 8p, 5d, 3f) and, for Au, (22s, 18p, 11d, 6f). These all-electron basis sets included f functions, which we found to be important in the CCSD(T) calculations for dimers.

The importance of accounting for relativistic effects may be observed by comparing the Local Density Approximation (LDA) calculations with and without relativistic effects for both dimers in Tables 1 and 2. Inclusion of the relativistic effect decreased the Cu–Cu bond length by an insignificant 0.029 Å for TZ2P and 0.028 Å for QZ4P. The effect is remarkably large for Au₂, with a decrease of 0.157 Å in bond length for TZ2P and 0.223 Å for QZ4P. The calculated Au₂ bond length with relativistic effects was significantly improved when compared with the experimental value of 2.472 Å.

Although inclusion of the relativistic effect significantly improved the calculated bond length for the gold dimer, the LDA binding energies remained greater than the accepted values. Binding energy errors were approximately 0.7 eV for Cu₂ and 0.6 eV for Au₂. This is the well-known overbinding effect of the LDA. Therefore, we also tested several general gradient corrections, so that nonlocal exchange and correlation

effects were included. The general gradient methods included the exchange and correlation corrections of Perdew and Wang³⁰ (PW91), the exchange and correlation corrections proposed by Perdew, Burke, and Ernzerhof³¹ (PBE), the revised PBE exchange correction reported by Hammer, Hansen, and Norskov³² with the Perdew–Burke–Ernzerhof³¹ correlation correction (RPBE), the revised PBE exchange correction of Zhang and Wang³³ with the Perdew–Burke–Ernzerhof³⁴ correlation correction (revPBE), and the gradient correction developed³⁴ by Becke with the Lee–Yang–Parr 1988^{35–37} correlation correction (BLYP). The computational results for the two dimers are compared with the experimental data in Tables 1 and 2.

For all of the GGA methods, the results from the TZ2P and QZ4P basis sets were similar, but the QZ4P result was slightly improved for Au₂. The Au₂ bond length decreased and that for Cu₂ increased for all the GGA methods. The slightly overall better performance of QZ4P over TZ2P was expected, as QZ4P is the largest basis set in the ZORA directory, has a large number of polarization functions for the atoms, and was intended for near basis set limit calculations on small systems. Tests performed on many small molecules have shown that for properties such as binding energies, the QZ4P basis set provided results close to those obtained in the literature with very large GTO basis sets.^{37,38} Based on the observations in Tables 1 and 2, the QZ4P basis set was chosen for the trimer PES calculations.

From the data in Table 1, one observes that the PBE and PW91 methods provide similar results for copper, in excellent agreement with experiment for both the TZ2P and QZ4P basis sets. A choice between the two methods is arbitrary, but we have selected the PW91 DFT method for the trimer studies. The PW91 results were in excellent agreement with the calculated bond lengths and harmonic frequencies from the CCSD(T)/StECP(2f) theoretical method; the relative error was less than 0.5% for bond length, and less than 2.5% for harmonic frequencies. In the case of Au₂, the PW91 bond length and binding energy are in better agreement with experimental values than the CCSD(T) results. These results provided confidence in the application of the method to the trimers. In particular, the dimer bond length would be an important parameter in the fitting process for the trimer BO surface, and frequency calculations were critical to differentiate the static Jahn–Teller distortion from a dynamic effect. Although the binding energy for the Cu₂ was approximately 0.3 eV larger than the CCSD(T) result and about 0.2 eV larger than the experimental value, this overbinding was not important because we employed *relative* energies among the trimer conformations in calculating the potential surfaces. These calculations were designated as PW91/ZORA-QZ4P.

To test the spin–orbit coupling effect, we included spin–orbit coupling calculations for both dimers and trimers. Because the current version of ADF does not support spin-unrestricted calculations, all of the spin–orbit coupling calculations in the paper were spin-restricted open shell, spin–orbit coupled DFT calculations. In addition, the optimized dimer bond lengths and trimer geometries that included spin–orbit coupling were obtained by single point calculations at a series of different geometries. These calculations are designated as PW91/ZORA-QZ4P(spín–orbit). From Tables 1 and 2, it may be observed that the spin–orbit effects were small for both dimers. The small effects were as expected, because both dimers have closed shells and the bonding was mainly due to the atomic *ns* orbital. This orbital was not affected by spin–orbit coupling. As van Lenthe et al.²⁸ pointed out in the case of Au₂, the remaining small spin–orbit effect arose from the mixing of 6p character into the

TABLE 3: Parameters for the BO Analytical Potential (in 10^{−3} au)

parameter	Cu ₃	Au ₃	Au ₃ (spin–orbit)
<i>d</i> ₀	−83.062106	−85.704353	−88.463165
<i>R</i> ₀	4182.0659	4750.9563	4739.4328
<i>a</i> ₁	1508.7382	1551.7705	1495.1774
<i>a</i> ₂	622.17988	543.15480	449.97811
<i>a</i> ₃	191.61196	162.69206	122.29176
<i>c</i> ₁	−26.049673	737.19042	520.75374
<i>c</i> ₂	−333.25624	1275.6882	940.20518
<i>c</i> ₃	596.34265	−195.27131	−55.432907
<i>c</i> ₄	185.99625	−150.50150	−102.38484
<i>b</i> ₁	109.69951	120.26567	116.39461
<i>b</i> ₂	76.034100	−38.599315	−53.293013
<i>b</i> ₃	47.427405	−34.649015	10.323165
<i>b</i> ₄	12.761350	191.37891	38.578784
<i>b</i> ₅	0.59223642	0.60950052	−0.21006720
<i>b</i> ₆	−3.6982922	−0.32173852	6.2755544
<i>b</i> ₇	5.7862211	39.848070	10.695885
<i>b</i> ₈	1.0407547	−112.63300	−44.876219
<i>b</i> ₉	−60.153507	97.247572	106.05723
<i>b</i> ₁₀	−0.10064858	−2.3740101	0.93480156
<i>b</i> ₁₁	23.906416	75.061704	−7.6436669

(6s+6s) bonding orbit and the mixing of 6s character into the 5d shells. At shorter distances, there was greater 6p mixing, which increased the spin–orbit stabilization. Therefore, spin–orbit coupling will slightly shorten the bond length of Au₂ and increase its binding energy. The same reasoning may be applied to Cu₂, but of course in this case, copper has a smaller effective nuclear charge and, thus, a smaller spin–orbit effect and bond length shortening. We postpone the discussion of trimers until the next section.

c. Analytic Potential. For the BO surfaces, the analytic form of the adiabatic potential energy surface was chosen to be similar to that used by Gerber et al.³⁹ for the alkali metals and in our previous work involving the silver trimer.¹⁴ Because complete details were provided in our earlier paper, only a brief description is presented here. The potential is given by

$$E(Q_a, Q_x, Q_y) = V(|R_1 - R_2|) + V(|R_2 - R_3|) + V(|R_3 - R_1|) + [1 - \tanh G(Q_a, Q_x, Q_y)]F(Q_a, Q_x, Q_y)$$

where *E* is the energy with respect to three isolated atoms and (*Q*_{*a*}, *Q*_{*x*}, *Q*_{*y*}) are normal coordinates, defined on the basis of the *D*_{3h} geometry given by an equilateral triangle. The origin of the Cartesian coordinate system, in au, was chosen to be at the center of the equilateral triangle. *R*_{*j*} was the position of atom *j*. *V*(*R*) was a fit of the calculated potential energy curve of the dimer and had the following form:

$$V(R) = d_0(1 + a_1\Delta R + a_2\Delta R^2 + a_3\Delta R^3) \exp(-a_1\Delta R)$$

$\Delta R = R - R_0$, where *R*₀ was the optimized dimer bond length.

By trial and error, the forms of *G*(*Q*_{*a*}, *Q*_{*x*}, *Q*_{*y*}) and *F*(*Q*_{*a*}, *Q*_{*x*}, *Q*_{*y*}) were determined to be

$$G(Q_a, Q_x, Q_y) = C1Q_a + C2\rho + C3\rho^2 + C4Q_a^2$$

$$F(Q_a, Q_x, Q_y) = b_1 + b_2Q_a + b_3Q_a^2 + b_4\rho^2 + b_5\rho c + b_6\rho^2 c + b_7Q_a\rho c + b_8Q_a\rho^2 c + b_9\rho + b_{10}\rho c^2 + b_{11}Q_a\rho$$

$$\rho = \sqrt{Q_x^2 + Q_y^2}$$

$$c = 4(Q_x/\rho)^3 - 3(Q_x/\rho)$$

The fitting parameters are presented in Table 3. This formalism

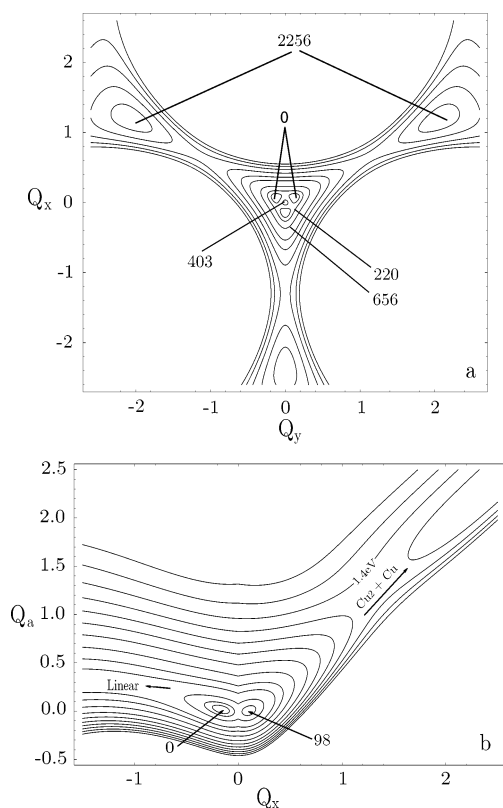


Figure 1. (a) Equipotential lines (energies in cm^{-1} , lines not equally spaced to highlight the features near the center) of the Cu_3 BO surface for $Q_a = 0$. The normal modes Q_x and Q_y form the basis for the e' representation in D_{3h} symmetry. The ${}^2E'$ equilateral and 2B_2 isosceles triangles are presented in the center. Local minima for the linear geometries are also shown. (b) Potential surface for the isosceles triangles, $Q_y = 0$. The dimer plus atom dissociation channel, the 2B_2 – 2A_1 pseudorotation, and the triangle-linear isomerization channel are shown.

provided the correct C_{3v} symmetry of the potential surface and allowed an accurate description, including the Jahn–Teller effect to second order, of both the dissociation limit and the neighborhood of the equilateral triangle.^{40,41}

III. Results and Discussion

a. Born–Oppenheimer Surfaces for the Trimers. Total energy calculations for ~ 100 configurations were obtained to construct the BO surface for each trimer. Because very stringent convergence criteria (10^{-8} au) were used in these calculations, the fitting error for any point on the surface was 10 cm^{-1} or less, with a root-mean-square error of 7.1 cm^{-1} . The reason for the residual fitting error was the limitation of the ADF program, or that of any computational chemistry software. Generally, the use of six or more significant figures in geometry parameters is meaningless. The equipotential lines, in cm^{-1} , for important BO surfaces in normal coordinate space are plotted in Figures 1 and 2 for Cu_3 and Au_3 , respectively. For the energy of the 2A_1 , 2B_2 , and ${}^2E'$ states, extrapolated values from the analytical potentials were obtained. To indicate that these values correspond to a specific geometry rather than the equipotential lines, the lines point to the center of the contour circles. All of the remaining values in the figures correspond to equipotential lines.

The BO surfaces for the two trimers have many features in common. Both I_B trimers are bound. In three-dimensional space, the surface is a warped Mexican hat.³⁹ For each trimer, the three equivalent 2B_2 isosceles triangle global minima are separated by 2A_1 isosceles triangle saddle points. The structures with linear

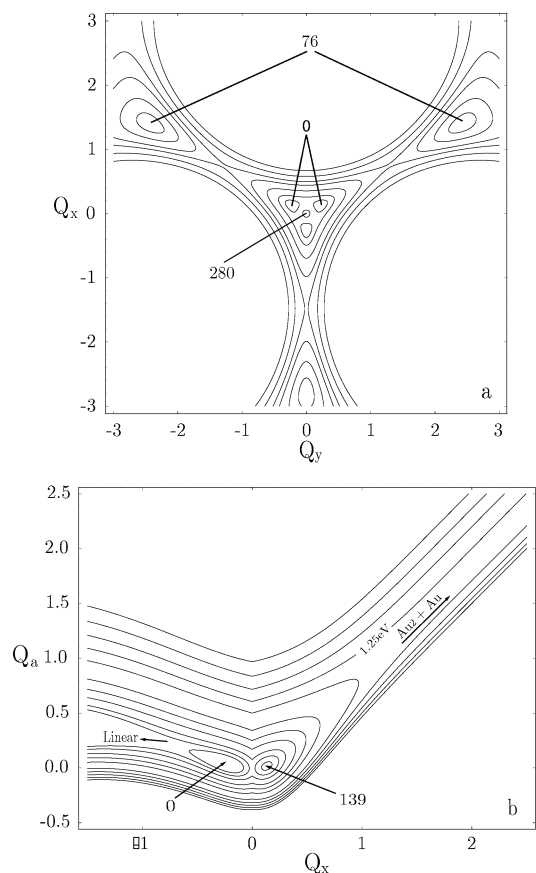


Figure 2. (a) Equipotential lines (energies in cm^{-1} , lines not equally spaced to highlight the features near the center) of the Au_3 BO surface for $Q_a = 0$. The normal modes Q_x and Q_y form the basis for the e' representation in D_{3h} symmetry. The ${}^2E'$ equilateral and 2B_2 isosceles triangles are presented in the center. Local minima for the linear geometries are also shown. (b) Potential surface for the isosceles triangles, $Q_y = 0$. The dimer plus atom dissociation channel, the 2B_2 – 2A_1 pseudorotation, and the triangle-linear isomerization channel are shown.

geometry are higher in energy than the global 2B_2 minima. The equilateral triangle geometry, shown in the center of Figures 1a and 2a, is also higher in energy than the 2B_2 structures. There is a reaction path connecting the 2B_2 minimum with the linear geometry local minimum. In Figures 1b and 2b, both the pseudorotation barrier and a dissociation pathway are evident. The dissociation pathway represents the reaction of trimer to dimer plus atom. The fact that the trimers are bound differs from the analogous hydrogen trimer, which is unstable with respect to dissociation. The dissociation energies of the copper and gold trimers are at least a factor of 2 greater than those for the alkali trimers. The added stability of these two trimers is due to the d -electron contribution to the bonding.

b. Cu_3 . (1) Potential Surface without Spin–Orbit Coupling. The individual potential surfaces reflect differences in the physical properties of the clusters. In Figure 1a, Cu_3 is seen to have a Jahn–Teller stabilization energy of 403 cm^{-1} and the linear form of the trimer lies 2256 cm^{-1} above the 2B_2 isosceles triangle isomer. Figure 1b indicates a pseudorotation barrier, the energy difference between the 2A_1 state and the 2B_2 state, of 98 cm^{-1} , and a dissociation energy of 1.4 eV .

(2) Optimized Geometries for the Surface Minima. As a test of the quality of the surface, several important geometries were fully optimized with the same theoretical method (PW91/ZORA-QZ4P) used to generate the potential surface. The results are given in the first four rows of Tables 4. A comparison of these

TABLE 4: Calculated Geometries for Cu₃^a

state	symmetry	<i>r</i> , Å	<i>r</i> _{base} , Å	apex angle, deg	symmetric stretch, cm ⁻¹	bend, cm ⁻¹	<i>E</i> ₀ , cm ⁻¹	<i>E</i> ₁ ^b , cm ⁻¹	<i>D</i> _e , eV
² E'	<i>D</i> _{3h}	2.328	2.328	60.00	264	161	293	411	
² A ₁	<i>C</i> _{2v}	2.384	2.241	56.08	274	191	232	102	
² B ₂	<i>C</i> _{2v}	2.275	2.489	66.34	270	125	273	0	1.444
² Σ _u ⁺	<i>D</i> _{∞h}	2.277	2.277	180.00	267	169	218	2265	
E _{5/2}	<i>D</i> _{3h}	2.328		60.00			0		
E _{3/2}	<i>D</i> _{3h}	2.328					246		
<i>J</i> _{1/2u}	<i>D</i> _{∞h}	2.277		180.00			2020		
² A ₁	<i>C</i> _{2v}	2.444	2.283	55.68				153	
² B ₂	<i>C</i> _{2v}	2.283	2.501	66.43				0	1.135
² Σ _u ⁺	<i>D</i> _{∞h}	2.294		180.00				2642	
² A ₁ ^c	<i>C</i> _{2v}	2.515	2.319	54.91	224	151		171	
² B ₂ ^c	<i>C</i> _{2v}	2.368	2.664	68.48	213	109		0	

^a The results in the first four rows were obtained using PW91/ZORA-QZ4P. Results in rows five through seven were calculated using PW91/ZORA-QZ4P(spín-orbit), and the CCSD(T)/StECP(2f) theoretical method was used for the results in rows eight through ten. ^b All the energies are with respect to the ²B₂ energy. ^c From ref 42, SDCI results.

tables with Figure 1 indicates that the Jahn–Teller stabilization energies for the ²B₂ isosceles triangle global minima, the ²A₁ isosceles triangle saddle point energies and the dissociation energies are in good agreement with the values from the analytic potential; the analytic potential fitting errors are insignificant. For Cu₃, the optimized PW91/ZORA-QZ4P results, shown in Table 4, indicate a Jahn–Teller stabilization energy of 411 cm⁻¹, a zero point energy of 273 cm⁻¹, and a pseudorotation barrier of 102 cm⁻¹. Because the pseudorotation barrier is smaller than its zero-point energy, the Cu₃ cluster is a Jahn–Teller fluxional molecule that has hindered pseudorotations among the three equivalent ²B₂ states. The CCSD(T)/StECP(2f) results are provided in rows eight through ten of the table. For some parameters, the agreement with the DFT results is very good. For example, bond length differences are less than 2%. There is reasonable agreement between the ab initio and DFT barriers for pseudorotation and isomerization to the linear structure. Our calculated DFT Jahn–Teller distortion energy and pseudorotation barrier are also in reasonable agreement with the SDCI+Q results found in the literature⁴² and shown in the last two rows of Table 4.

The CCSD(T) pseudorotation barrier is approximately 50 cm⁻¹ greater than the DFT derived barrier and the CCSD(T) barrier to isomerization is approximately 300 cm⁻¹ greater than that from DFT. A discrepancy of much greater magnitude was reported for the *C*_{2v} to linear isomerization of P₃.²² For that trimer the CCSD(T) isomerization barrier was more than 6000 cm⁻¹ higher than that from DFT. No rationale for this observation was proposed, and the source of the difference remains unclear. The biggest discrepancy between the DFT and CCSD(T) results lies in the dissociation energy of the trimer, the DFT binding energy for the ²B₂ state is about 0.3 eV (30%) greater than the ab initio result and the source of the difference remains unclear.

Because Jahn–Teller coupling and spin–orbit coupling both involve electron angular momentum, a consideration of the geometry of any nonsinglet degenerate state must consider both effects. Typically, the two effects have opposite actions on the geometry. In other words, the spin–orbit coupling might quench the Jahn–Teller distortion, if the spin–orbit splitting is much larger than the Jahn–Teller stabilization energy. When considering spin–orbit coupling, the *D*_{3h} symmetry turns into the *D*_{3h}² double group symmetry, and the ²E' electronic state in *D*_{3h} symmetry is split into E_{3/2} and E_{5/2} spin–orbit components, where the E_{3/2} component has the lower energy. The optimized PW91/ZORA-QZ4P(spín-orbit) geometry corresponding to the

E_{5/2} spin–orbit state and the spin–orbit splitting are displayed in Table 4, rows five through seven.

Comparing the PW91/ZORA-QZ4P(spín-orbit) optimized geometry with that from PW91/ZORA-QZ4P, there is no difference in bond length and the spin–orbit splitting, 246 cm⁻¹, is only about half of the Jahn–Teller distortion energy for the ²B₂ state. This indicates that the spin–orbit coupling does not quench the Jahn–Teller effect for the copper trimers. Thus, we conclude that the potential surface for Cu₃ without spin–orbit coupling shown in Figure 1 is a good approximation to the true potential surface.

c. Au₃. (1) Potential Surface without Spin–Orbit Coupling. Figure 2a indicates a Jahn–Teller stabilization energy of 280 cm⁻¹, much less than that for Cu₃. The linear isomer is nearly degenerate with the ²B₂ isosceles triangle minima; only 76 cm⁻¹ separates the two configurations. Figure 2b shows that the pseudorotation barrier of 139 cm⁻¹ is larger than that of Cu₃, but that the dissociation energy, 1.25 eV, is comparable to that of Cu₃.

(2) Optimized Geometries for the Surface Minima. For Au₃, the optimized PW91/ZORA-QZ4P calculations shown in Table 5 predict a ²B₂ state Jahn–Teller stabilization energy that is 271 or 106 cm⁻¹ greater than the zero-point energy. The pseudorotation barrier is 143 cm⁻¹, which is smaller than the zero-point energy for the ²B₂ state. Therefore, one might expect the Au₃ cluster to also be a fluxional molecule around its global minimum much as Cu₃. This is also evident in the BO surface (Figure 2), where the potential surface is quite flat near the center. The linear structure is only 67 cm⁻¹ higher in energy than the ²B₂ state. This linear structure is also nearly degenerate with the ²A₁ state. The CCSD(T)/StECP(2f) results are also provided in Table 5. The agreement with the DFT results for the bond lengths and dissociation energy is very good (0.2% and 3%, respectively). The agreement of the isomerization and pseudorotation barriers from the two theoretical techniques is quite poor. There are previous calculations with which we may compare our results. The bond lengths from CASSCF calculations¹¹ agree well with our DFT and CCSD(T)/StECP(2f) results; however the CASSCF pseudorotation barrier lies between the values from our two theoretical methods.

Among the three I_B trimers, Au₃ is the most intriguing. As was true for all of the trimers, the orbitally degenerate ²E', *D*_{3h} ground state can undergo Jahn–Teller distortion that results in two states of *C*_{2v} symmetry, the ²A₁ and ²B₂ states. However, because gold is a heavy atom, spin–orbit coupling could conceivably quench this distortion, as these two effects are in competition. Previous self-consistent field modified coupled pair

TABLE 5: Calculated Geometries for Au₃^a

state	symmetry	r , Å	r_{base} , Å	apex angle, deg	symmetric stretch, cm ⁻¹	bend, cm ⁻¹	E_o , cm ⁻¹	E^b , cm ⁻¹	D_e , eV
² E'	D_{3h}	2.664						271	
² A ₁	C_{2v}	2.718	2.575	56.55	168	110	139	143	
² B ₂	C_{2v}	2.608	2.838	65.91	175	96	165	0	1.253
² Σ _u ⁺	$D_{\infty h}$	2.573		180.00	168	105	140	67	
E _{5/2}	D_{3h}	2.643		60.00			0		
E _{3/2}	D_{3h}	2.643		60.00			2097		
$J_{3/2g}$	$D_{\infty h}$	2.497		180.00			44		
² A ₁	C_{2v}	2.719	2.565	56.29				50	
² B ₂	C_{2v}	2.607	2.798	64.93				0	1.302
² Σ _u ⁺	$D_{\infty h}$	2.578		180.00				1370	
² A ₁ ^c	C_{2v}	2.72	2.57	56.4				81	
² B ₂ ^c	C_{2v}	2.60	2.82	65.7				0	
² A ₁ ^d	C_{2v}	2.79	2.60	55.6				45	
² B ₂ ^d	C_{2v}	2.65	2.90	66.4				0	

^a The results in the first four rows were obtained using PW91/ZORA-QZ4P. Results in rows five through seven were calculated using PW91/ZORA-QZ4P(spin-orbit), and the CCSD(T)/StECP(2f) theoretical method was used for the results in rows eight through ten. ^b All the energies are with respect to the ²B₂ energy. ^c From ref 11, CASSCF/POLCI + spin-orbit coupling results. ^d From ref 43, relativistic configurations (RECI) results.

TABLE 6: Mulliken Spin Populations for Both Trimers (QZ4P)^a

state		charge	net spin	s	p	d	f	unpaired s spin	unpaired s spin (exp) ^a	dipole moment, D	
Cu ₃	² B ₂	center	0.1298	0.0756	6.7591	12.2023	9.9006	0.0082	-0.007	-0.026	
		end	-0.0649	0.4622	7.0510	12.1434	9.8641	0.0064	0.43	0.29	
		total			20.8611	36.4891	29.6288	0.021			0.67
² A ₁	center	-0.1513	0.6044	7.1807	12.1206	9.8432	0.0067				
	end	0.0756	0.1978	6.8478	12.182	9.8872	0.0073			-0.82	
Au ₃	² B ₂	center	0.0369	0.0440	10.8635	24.2068	29.8662	14.0266	-0.014	-0.056	
		end	-0.0185	0.4780	11.0138	24.1789	29.8084	14.0174	0.39	0.39	
		total			32.8911	72.5646	89.4830	42.0614			0.95
² A ₁	center	-0.060.77	0.6559	11.0886	24.1908	29.7729	14.0155				
	end	0.0338	0.1721	10.8747	24.2191	29.8488	14.0235			-1.17	

^a Unpaired s spin populations calculated from ESR experimental data, ref 7.

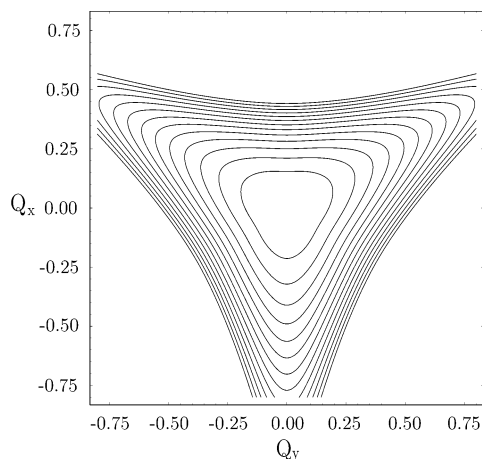


Figure 3. Equipotential lines (contour spacing 0.08 eV; contour at largest Q_x corresponding to -2.72 eV) of the Au₃ BO surface for $Q_a = 0$. The normal modes Q_x and Q_y form the basis for the e' representation in D_{3h} symmetry.

functional (SCF-MCP)⁴² calculations reported a ²B₂-²A₁ energy separation of 45 cm⁻¹, with the ²B₂ state as the ground state. The first observation of the gold trimer by electron spin resonance in a C₆D₆ matrix⁷ also reported the ground state of Au₃ as the ²B₂ electronic state with C_{2v} symmetry. The unpaired electron was said to be localized on the terminal atoms. The results of our work without spin-orbit coupling are consistent with these observations in that they predict a small pseudoro-

tation barrier as well as a small Jahn-Teller stabilization energy. Recently, Guo et al.¹⁵ obtained the vibronic absorption spectrum and calculated the spin-orbit splitting of the ground state. They concluded that the spin-orbit splitting is larger than the Jahn-Teller stabilization energy, and thus, the spin-orbit coupling quenches the distortion, resulting in a D_{3h} minimum for the ground electronic state of Au₃. This calculation, as well as one involving the excited electronic states^{43,44} of Au₃, appear to be the only predictions of the spin-orbit coupling dominance over the Jahn-Teller Effect. However, these calculations are in agreement with the most recent (and highest quality) experimental results. It is clear that our current calculations must also test the importance of spin-orbit coupling.

Following the procedure employed for Cu₃, we obtained the PW91/ZORA-QZ4P(spin-orbit) optimized geometry corresponding to the E_{5/2} spin-orbit state and calculated the spin-orbit splitting for Au₃ under the D_{3h}^2 double group symmetry. The results are shown in Table 5. Comparing the PW91/ZORA-QZ4P(spin-orbit) optimized geometry with that of the PW91/ZORA-QZ4P, one observes an approximately 0.02 Å shortening in bond length for the former. This trend is identical to that observed for the dimers; the spin-orbit effect tended to shorten the bond length and the effect was greater for Au than for Cu. The spin-orbit splitting is 2097 cm⁻¹, which lies close to the band observed at 2025.5 cm⁻¹ in laser-ablated gold experiments. This feature was assigned to the spin-orbit splitting of Au₃ by Guo et al.¹⁵ Spin-orbit coupling is approximately 8 times greater than the Jahn-Teller distortion energy for the ²B₂ state.

The spin-orbit effect stabilizes the D_{3h} structure and quenches the Jahn-Teller distortion in Au_3 . Thus, we believe the potential surface for Au_3 shown in Figure 2 without spin-orbit coupling is a poor approximation to the actual potential surface. To obtain a true representation of the PES, one must include spin-orbit effects.

(3) *Potential Surface with Spin-Orbit Coupling.* To understand the effect of spin-orbit coupling on the shape of the surface, one must plot the Au_3 surface with spin-orbit coupling included. The analytical potential has the same form as that used above and (Q_a, Q_x, Q_y) are defined on the basis of the optimized D_{3h} geometry from the single point calculations at different (equilateral) bond lengths. The state for the single atom is chosen to be the lowest $|JM_J\rangle$ in the fully relativistic ZORA plus spin-orbit case. Because of the use of approximate spin-restricted open shell, spin-orbit coupled DFT calculations, one may only optimize the D_{3h} bond length up to the nearest 0.001 Å and the binding energy is not sufficiently accurate for quantitative use; the surface is valid for qualitative use. The root-mean-square fitting error is approximately 2.5 meV. The surface near the optimized D_{3h} geometry is shown in Figure 3, with 0.08 eV contour spacing, and the contour at the largest Q_x corresponds to -2.72 eV (with respect to three isolated atoms). One observes that near the optimized D_{3h} geometry, the surface is quite flat and the spin-orbit effect indeed stabilizes the D_{3h} structure and quenches the Jahn-Teller distortion.

d. Mulliken Population Analysis and ESR Properties. For both trimers, the spin populations from the PW91/ZORA-QZ4P calculations are shown in Table 6. The PW91/ZORA-QZ4P calculation is sufficient, even for Au_3 (without the spin-orbit effect) because in most of the ESR experiments the Jahn-Teller distortion was observed, probably as a result of matrix effects. In the 2B_2 electronic ground state, the unpaired electron is localized mainly on the terminal atoms, whereas the opposite is true for the 2A_1 state. The calculated unpaired s spins for the 2B_2 states may be compared with the values derived from ESR experiments. In the calculations, the central atom has a small negative s spin population that is due to spin polarization, as observed in the experiment for the 2B_2 state.

Although bonding in the ground state of the coinage metals arises primarily from a single s electron on each atom, the metal d orbitals contribute as well because they are involved in electron correlation. This may be seen in the d electron populations for the 2B_2 ground state of both trimers in Table 6. The gold trimer has a slightly lower valence d electron population than copper. The rationale for this ordering is that gold has larger relativistic effects. The large nuclear charge on gold causes the $6s$ electron to penetrate close to the nucleus. The orbital will undergo a relativistic contraction and is significantly stabilized. The outer d and f orbitals are better shielded by the more contracted s orbitals and undergo a relativistic expansion. This relativistic effect is reflected in the excitation energies of the atoms from the ground state. The $3d^{10}4s^1$ (2S) to $3d^94s^2$ ($^2D_{1/2}$) excitation energy for Cu is 1.39 eV and the analogous Au excitation energy from $5d^{10}6s^1$ (2S) to $5d^96s^2$ ($^2D_{1/2}$) is 1.14 eV.⁴⁵ The lower excitation energy for Au leads to a significant admixture of $5d^96s^2$ character and results in a lower valence d population in our calculations. To make the comparison complete, Table 6 also contains the dipole moments of the trimers. The values are larger for Au_3 in both the 2A_1 and 2B_2 states. For the 2B_2 state, the sign of the dipole moment is positive, but for the 2A_1 state, the dipole moment is negative.

IV. Summary

We have employed the PW91 theoretical method to obtain Born-Oppenheimer surfaces for copper and gold trimers. With a few exceptions, the physical parameters from the analytic surfaces agree well with those from optimized geometries using the same technique as well as those from a CCSD(T)/StECP(2f) calculation. Comparison is also made with the available experimental and theoretical results from the literature. Cu_3 is a Jahn-Teller fluxional molecule and the spin-orbit coupling is smaller than the Jahn-Teller effect. Spin-orbit coupling is significant for Au_3 and quenches the Jahn-Teller distortion in agreement with the computations of Guo et al.¹⁵ The calculated Mulliken populations are in agreement with the results of ESR experiments.

Acknowledgment. We acknowledge helpful discussions with Professor Robert Ditchfield.

References and Notes

- (1) Tani, T. *Phys. Today* **1989**, *42*, 36.
- (2) Leisner, T.; Rosche, C.; Wolf, S.; Granzer, F.; Woeste, F. L. *Surf. Rev. Lett.* **1996**, *3*, 1105.
- (3) Morse, M. D.; Hopkins, J. B.; Langridge-Smith, P. R. R.; Smalley, R. E. *J. Chem. Phys.* **1983**, *79*, 5316.
- (4) Vajda, S.; Wolf, S.; Busolt, U.; Hess, H.; Leisner, T.; Woste, L. *Springer Ser. Chem. Phys.* **1998**, *63* (Ultrafast Phenomena XI), 482.
- (5) DiLella, D. P.; Taylor, K.; Moskovits, M. *J. Phys. Chem.* **1983**, *87*, 524.
- (6) Haslett, T. L.; Bosnick, K. A.; Fedrigo, S.; Moskovits, M. *J. Chem. Phys.* **1999**, *111*, 6456.
- (7) Howard, J. A.; Sutcliffe, R.; Mile, B. *Surf. Sci.* **1985**, *156*, 214.
- (8) Bachmann, C.; Demuyneck, J.; Veillard, A. *Stud. Surf. Sci. Catal.* **1980**, *4* (Growth Prop. Met. Clusters: Appl. Catal. Photogr. Process), 269.
- (9) Langhoff, S. R.; Bauschlicher, C. W., Jr.; Walch, S. P.; Laskowski, B. C. *J. Chem. Phys.* **1986**, *85*, 7211.
- (10) Flad, J.; Igel-Mann, G.; Preuss, H.; Stoll, H. *Chem. Phys.* **1984**, *90*, 257.
- (11) Balasubramanian, K.; Liao, M. Z. *Chem. Phys.* **1988**, *127*, 313.
- (12) Walch, S. P.; Bauschlicher, C. W., Jr.; Langhoff, S. R. *J. Chem. Phys.* **1986**, *85*, 5900.
- (13) Yoon, J.; Kim, K. S.; Baeck, K. K. *J. Chem. Phys.* **2000**, *112*, 9335.
- (14) Shen, Y.; BelBruno, J. J. *J. Chem. Phys.* **2003**, *118*, 9241.
- (15) Guo, R.; Balasubramanian, K.; Wang, X.; Andrews, L. *J. Chem. Phys.* **2002**, *117*, 1614.
- (16) Balasubramanian, K.; Liao, M. Z. *J. Chem. Phys.* **1987**, *86*, 5587.
- (17) Frisch, M. J.; Trucks, G. W.; Schlegel, H. B.; Scuseria, G. E.; Robb, M. A.; Cheeseman, J. R.; Zakrzewski, V. G.; Montgomery, J. A., Jr.; Stratmann, R. E.; Burant, J. C.; Dapprich, S.; Millam, J. M.; Daniels, A. D.; Kudin, K. N.; Strain, M. C.; Farkas, O.; Tomasi, J.; Barone, V.; Cossi, M.; Cammi, R.; Mennucci, B.; Pomelli, C.; Adamo, C.; Clifford, S.; Ochterski, J.; Petersson, G. A.; Ayala, P. Y.; Cui, Q.; Morokuma, K.; Malick, D. K.; Rabuck, A. D.; Raghavachari, K.; Foresman, J. B.; Cioslowski, J.; Ortiz, J. V.; Stefanov, B. B.; Liu, G.; Liashenko, A.; Piskorz, P.; Komaromi, I.; Gomperts, R.; Martin, R. L.; Fox, D. J.; Keith, T.; Al-Laham, M. A.; Peng, C. Y.; Nanayakkara, A.; Gonzalez, C.; Challacombe, M.; Gill, P. M. W.; Johnson, B.; Chen, W.; Wong, M. W.; Andres, J. L.; Gonzalez, C.; Head-Gordon, M.; Replogle, E. S.; Pople, J. A. *Gaussian 98*, Revision A.11; Gaussian, Inc.: Pittsburgh, PA, 1998.
- (18) Andrae, D.; Hausermann, U.; Dolg, M.; Stoll, H.; Preuss, H. *Theor. Chim. Acta* **1990**, *77*, 123.
- (19) Bauschlicher, C. W., Jr.; Langhoff, S. R.; Partridge, H. *J. Chem. Phys.* **1990**, *93*, 8133.
- (20) Kaplan, I. G.; Santamaria, R.; Novaro, O. *Int. J. Quantum Chem., Quantum Chem. Symp.* **1993**, *27*, 743.
- (21) Huber, K. P.; Herzberg, G. *Constants of Diatomic Molecules*; Van Nostrand Reinhold: New York, 1979; Vol. 4.
- (22) Choi, H.; Park, C.; Baeck, K. K. *J. Phys. Chem. A* **2002**, *106*, 5177.
- (23) te Velde, G.; Bickelhaupt, F. M.; Baerends, E. J.; Fonseca Guerra, C.; van Gisbergen, S. J. A.; Snijders, J. G.; Ziegler, T. *J. Comput. Chem.* **2001**, *22*, 931.
- (24) Lee, Y. S.; Ermler, W. C.; Pitzer, K. S. *J. Chem. Phys.* **1979**, *70*, 288.
- (25) van Lenthe, E.; Ehlers, A. E.; Baerends, E. J. *J. Chem. Phys.* **1999**, *110*, 8943.
- (26) van Lenthe, E.; Baerends, E. J.; Snijders, J. G. *J. Chem. Phys.* **1993**, *99*, 4597.

- (27) van Lenthe, E.; Baerends, E. J.; Snijders, J. G. *J. Chem. Phys.* **1994**, *101*, 9783.
- (28) van Lenthe, E.; Snijders, J. G.; Baerends, E. J. *J. Chem. Phys.* **1996**, *105*, 6505.
- (29) van Lenthe, E.; et al. *Int. J. Quantum Chem.* **1996**, *57*, 281.
- (30) Perdew, J. P.; Chevary, J. A.; Vosko, S. H.; Jackson, K. A.; Pederson, M. R.; Singh, D. J.; Fiolhais, C. *Phys. Rev.* **1992**, *B46*, 6671.
- (31) Perdew, J. P.; Burke, K.; Ernzerhof, M. *Phys. Rev. Lett.* **1996**, *77*, 3865.
- (32) Hammer, B.; Hansen, L. B.; Norskov, J. K. *Phys. Rev.* **1999**, *B59*, 7413.
- (33) Zhang, Y.; Yang, W. *Phys. Rev. Lett.* **1998**, *80*, 890.
- (34) Becke, A. D.; *Phys. Rev. A* **1988**, *38*, 3098.
- (35) Lee, C.; Yang, W.; Parr, R. G. *Phys. Rev.* **1988**, *B37*, 785.
- (36) Johnson, B. G.; Gill, P. M. W.; Pople, J. A. *J. Chem. Phys.* **1993**, *98*, 5612.
- (37) Russo, T. V.; Martin, R. L.; Hay, P. J. *J. Chem. Phys.* **1994**, *101*, 7729.
- (38) ADF document, "Basis sets for ADF and BAND", release 2002.01.
- (39) Gerber, W. H.; Schumacher, E. *J. Chem. Phys.* **1978**, *69*, 1692.
- (40) Martin, R. L.; Davison, E. R. *Mol. Phys.* **1978**, *35*, 1713.
- (41) Herzberg, G. *Electronic Spectra of Polyatomic Molecules*; Van Nostrand Reinhold: New York, 1979; Vol. 4.
- (42) Walch, S. P.; Laskowski, B. C. *J. Chem. Phys.* **1986**, *84*, 2734.
- (43) Bauschlicher, C. W., Jr. *Chem. Phys. Lett.* **1989**, *156*, 91.
- (44) Balasubramanian, K.; Das, K. K. *Chem. Phys. Lett.* **1991**, *186*, 577.
- (45) Moore, C. E. *Atomic Energy Levels*; National Bureau of Standards: Gaithersburg, MD, 1971.